bioRxiv preprint doi: https://doi.org/10.1101/2020.02.13.947903; this version posted February 13, 2020. The copyright holder for this preprint (which was not certified by peer review) is the author/funder. All rights reserved. No reuse allowed without permission.

Parallel processing of sensory cue and spatial information in the Dentate Gyrus

Sebnem N. Tuncdemir[1,2], Andres D. Grosmark[3], Gergely Turi[1,2], Amei Shank[4], Jack Bowler[3], Gokhan Ordek[2], Attila Losonczy[3], Rene Hen[1,2], Clay O. Lacefield[1,2,5*]

[1]Department of Psychiatry, Columbia University, New York, NY 10032, USA
[2]Division of Systems Neuroscience, New York State Psychiatric Institute, New York, NY 10032, USA
[3]Department of Neuroscience, Mortimer B. Zuckerman Mind Brain Behavior Institute, Columbia University, New York, NY 10027, USA
[4]Columbia College, New York, NY 10027, USA
[5]Lead Contact
*Correspondence: col8@cumc.columbia.edu

Abstract

During exploration, animals form a cognitive map of an environment by combining specific sensory cues or landmarks with specific spatial locations, a process which critically depends on the mammalian hippocampus. The dentate gyrus (DG) is the first stage of the canonical hippocampal trisynaptic circuit and plays a critical role in contextual discrimination, yet it remains unknown how neurons within the DG encode both spatial and sensory information during cognitive map formation. Using two photon calcium imaging in head fixed mice navigating a virtual linear track, along with on-line sensory cue manipulation, we have identified robust sensory cue responses in DG granule cells. Granule cell cue responses are stable for long periods of time, selective for the modality of the stimulus and accompanied by strong inhibition of the firing of other active neurons. At the same time, there is a smaller fraction of neurons whose firing is spatially tuned but insensitive to the presentation of nearby cues. These results demonstrate the existence of “cue cells” in addition to the better characterized “place cells” in the DG. We hypothesize that the observed diversity of representations within the granule cell population may support parallel processing of complementary sensory and spatial information.

Introduction

An animal’s location in an environment is highly relevant for guiding its behavior, both to find areas of potential reward and avoid areas of possible danger. During navigation, the mammalian hippocampal formation is thought to integrate self-motion and sensory information into a neural representation, or “cognitive map”, of an environment (O’Keefe and Dostrovsky, 1971). Many principal neurons in the hippocampus are active within a restricted area of space or “place field”, which collectively map the positions within a present environment and may underlie such an internal spatial map (O’Keefe and Nadel, 1978; Lisman et al., 2017). Yet it is still unclear how spatial information is combined with specific sensory cues to generate a cognitive map.

As the first layer in the hippocampal trisynaptic circuit, the dentate gyrus (DG) forms the initial stage in hippocampal information processing (Amaral et al., 2007). It receives long-range excitatory inputs largely from the lateral and medial entorhinal cortices (LEC and MEC,

bioRxiv preprint doi: https://doi.org/10.1101/2020.02.13.947903; this version posted February 13, 2020. The copyright holder for this preprint (which was not certified by peer review) is the author/funder. All rights reserved. No reuse allowed without permission.

respectively), and sends mossy fiber projections to area CA3 (Henze et al., 2000; Witter, 2007). Due to its large number of small, sparsely active principle neurons, or "granule cells", the DG has been suggested to orthogonalize similar input patterns into non-overlapping representations to prevent interference between features such as similar contexts or memories, a function known as pattern separation (Marr 1971; Treves and Rolls, 1994; *c.f.* van Dijk and Fenton, 2018).

There is also accumulating evidence for a role of the DG in binding together different types of information from its major inputs in the LEC and MEC (Kesner, 2013; Lee and Jung, 2017). The LEC is generally thought to represent information about sensory cues (Hargreaves et al., 2005), while the MEC is considered to encode self-motion information (Fyhn et al., 2004). Since individual granule cells receive projections from both of these areas on distinct zones of the same dendrites, the outer molecular layer for LEC and the middle molecular layer for MEC, these inputs have the potential to be the basis for dendritic computations that integrate sensory and self-motion information into a discrete spatial representation (McNaughton et al., 1978; Krueppel et al., 2011; Kim et al., 2018). In other hippocampal subareas however, emerging evidence suggests that principal neurons exhibit a significant degree of functional heterogeneity, such that multiple channels of information might remain distinct within a local population (Soltesz and Losonczy, 2018; Cembrowski and Spruston, 2019). It remains unclear whether sensory and spatial information are integrated, or remain separate, at the level of the DG.

We sought to examine how the DG participates in spatial map formation by recording calcium activity in large populations of granule cells in the mouse dorsal DG during head-fixed locomotion on a treadmill. By controlling the administration of sensory cues and their pairing with the animal's position on the treadmill, we were able to dissect sensory and spatial contribution to granule cell firing. We found that surprisingly most of the task-associated neurons were highly sensitive to specific sensory cues presented along the treadmill belt, rather than discrete locations. Cue responses in single neurons were stable for long periods of time, selective for the modality of the stimulus and accompanied by strong inhibition of the firing of other active neurons. At the same time, a smaller fraction of neurons exhibited spatial tuning independent of nearby cue presentation. These two channels of information, sensory and spatial, were largely distinct within the granule cell population, and led us to postulate the existence of "cue cells" in addition to the better characterized "place cells" of the region. This work suggests that the DG maintains a largely parallel code for cues in an environment and their location; yet, possesses specific points of integration, for example through mutual inhibition. Such properties may play a role in pattern separation and other functions of the dentate gyrus in hippocampal information processing.

Results

To investigate the interaction between sensory and spatial representations in the dentate gyrus (DG), we used two photon calcium imaging of large populations of granule cells in head-restrained mice running on a treadmill as a virtual linear track (Danielson et al., 2016, 2017). Mice were injected with rAAV.Syn.GCaMP6s to express the genetically encoded calcium indicator GCaMP6s in the dorsal DG followed by the implantation of a chronic imaging window above the hippocampal fissure, which allowed us to image the calcium dynamics of neurons in the granule

bioRxiv preprint doi: https://doi.org/10.1101/2020.02.13.947903; this version posted February 13, 2020. The copyright holder for this preprint (which was not certified by peer review) is the author/funder. All rights reserved. No reuse allowed without permission.

cell layer during treadmill behavior (Figure 1A). After habituation, mice were trained to run for water rewards on a 2m-long treadmill belt containing a narrow band at a fixed location as a lap transition cue (the edges of the linearized treadmill belt). Following run training, animals ran on a similar belt but with discrete sensory cues of different modalities presented at precise locations on the track, during 15 minute sessions (Figure 1B, methods). Movies of population calcium imaging data were motion corrected offline (Pnevmatikakis and Giovannucci, 2017), and the activity of putative single neurons was isolated (Pachitariu et al., 2016; Giovannucci et al., 2019). Neurons with significant spatial tuning of calcium activity along the track were identified using previously described methods (Danielson et al., 2016; Grosmark and Buzsáki, 2016), and in a subset of sessions activity of single neurons was tracked in multiple conditions over multiple sessions (Sheintuch et al., 2017).

In order to isolate other factors known to affect hippocampal activity such as rewards (Gauthier and Tank, 2018) and locomotion speed (Fuhrmann et al., 2015), water reward was delivered at a random position during every lap and the treadmill was motorized at a constant speed, adjusted for each mouse (motorized velocity = 10.11 $\pm$ 0.64 cm/s, self-driven velocity = 12.76 $\pm$ 2.45 cm/s). Under such conditions, there were no significant differences in the fraction of spatially selective neurons or their mean firing rates in mice running on the motorized treadmill compared to mice advancing the treadmill belt through self-driven locomotion (Figure S1A-B), however mean spatial tuning was higher in mice running on the motorized treadmill (Figure S1C).

To investigate the influence of discrete sensory cues on spatial representations within the granule cell population, we introduced a 1s odor pulse delivered in the middle of the track on each lap. Strikingly, we found that the majority of spatially selective neurons exhibited receptive fields around the lap boundary and middle locations, corresponding to the track edge cue and middle cue positions, respectively (Figure 1C, 57% of cells with peak activity within 10cm of cues, 43% >10cm from cues, $p<0.0001$, Mann-Whitney test). These neurons could however be place cells that are enriched at the locations of sensory stimuli, or alternately could be directly driven by the stimulus. To test this, the olfactory cue was omitted or shifted 1/4th of the track once every 3-5 trials interleaved throughout the session (41$\pm$ 2 total laps/session). Under these conditions, a majority of neurons normally active in the middle of the track shifted their firing position to match the new location of the odor in cue-shift trials (Figure 1D, middle) and exhibited reduced activity in cue-omitted trials (Figure 1D, right), compared with normal middle cue laps (n = 285 spatially tuned neurons from 8 mice). In contrast, neurons firing at locations corresponding to the invariant edge cue were unchanged in omit and shift laps. Across the population, average firing rates (Figure 1E) and spatial information (Figure S1D) of spatially tuned neurons were also higher in positions corresponding to sensory cues in the normal cue trials. On trials with a shifted middle cue, average firing rates increased within the new cue region (red, inset $p=0.0234$ Signed Rank Sum test), and decreased at the normal cue location on cue-omitted trials (blue, inset $p<0.00001$, Signed Rank Sum test compared to the corresponding positions during normal trials (Figure 1E, inset). Similar population responses were found in other imaging sessions in the same regions when the olfactory cue was replaced with cues of other sensory modalities, such as tactile or visual cues (Figure S1E-H). Thus, the majority of spatially tuned neurons in the virtual linear track

bioRxiv preprint doi: https://doi.org/10.1101/2020.02.13.947903; this version posted February 13, 2020. The copyright holder for this preprint (which was not certified by peer review) is the author/funder. All rights reserved. No reuse allowed without permission.

environment are in fact active directly in response to presentation of cues at those locations, rather than the locations themselves.

Given these results, we divided the spatially tuned population into three groups for subsequent analyses based on the position of their spatial fields and their activity during cue manipulation (omit or shift) trials. The three response types are illustrated for one session (Figure 1F): 1) cells with spatial fields within the middle cue region that closely track the changes in cue presentation ("odor-cue cells", top); 2) cells with spatial fields around the lap boundary cue on the treadmill belt ("lap-cue cells", middle); and 3) the remaining spatially tuned cells with receptive fields outside of the cue locations throughout the track ("place cells", bottom). These three groups, odor-cue, lap-cue, and place cells, constituted 22.5±2%, 47.1±2% and 30.4±1% of the spatially tuned cells, respectively (Figure S1I,J). We found that cells with similar response types did not cluster together spatially within the imaging field and the groups did not exhibit significant differences in overall mean firing rates (Figure S1K,L). Spatial coding properties however differed between cue and place coding populations of neurons. Both population of cue cells showed higher average spatial information (Figure 1G, χ^2=48.47, p<0.0001, Kruskal-Wallis test) and had more consistent spatial firing between the first and the second half of each session than place cells (Figure 1H, χ^2=32.60, p<0.0001, Kruskal-Wallis test).

To probe the emergence of location specific firing in these populations, we identified the lap in which responses began to robustly occur within the preferred spatial field during the first session of exposure to the odor cue (spatial field onset lap (Sheffield et al., 2017)). We found that the majority of spatial fields of odor and lap cue cells appeared within the first five laps (38/65 (58%), 75/136 (55%), respectively) while the majority of spatial fields of place cells emerged later in the session (52/84 (62%) within 10 laps, Figure 1I, χ^2=9.29, p=0.0096, Kruskal-Wallis test). These results demonstrate that sensory cue representations are more reliable and appear with less exposure than place cell representations.

To further characterize the stability and coding specificity among these populations of granule cells, we investigated the responses of individual neurons over time and with respect to different sensory cues (Figure 2A, B). We utilized an analytical method (Sheintuch et al., 2017) to track cells over multiple sessions and were able to find significant numbers of the same cells active in sessions within a day or 1 week later in the same fields of view (Figure S2A,B). Although not all cells were identified in every session, a similar percentage of spatially selective neurons was registered in all sessions, which was confirmed by visual inspection to ensure that cells appeared consistent in the anatomical images (Figure S2C-G).

Between any two sessions, over days or cue modality, the cells encoding the invariant lap cue were the largest fraction of cells with similar response type (Figure 2C). Middle cue cells fired reliably to the olfactory cue over long periods of time, but were largely unresponsive to cues of other modalities presented at the same position (at chance levels p=0.6512 and significantly reduced fraction of overlapping cells compared to other response types χ^2=19.78, p<0.00001, Kruskal-Wallis test). Conversely, a lower percentage of place cells maintained their spatial tuning across days compared to cue cells recorded in the same sessions (χ^2=14.36, p<0.001, Kruskal-

bioRxiv preprint doi: https://doi.org/10.1101/2020.02.13.947903; this version posted February 13, 2020. The copyright holder for this preprint (which was not certified by peer review) is the author/funder. All rights reserved. No reuse allowed without permission.

Wallis test). Further comparisons between the cue and place representation types (i.e. whether cue cells become place cells or vice versa) over time or between sessions containing different sensory cues revealed a remarkable stability (Figure 2D, $p<0.001$, Rank Sum test), suggesting that cue and place representations remain largely stable within the DG.

We also quantified how spatial firing rates for individual registered cells were correlated over time and with respect to different sensory cues (Figure 2E). For this analysis, we computed the Pearson's correlation of spatial activity between registered cells within a day and across days, using the firing rate maps and cell type classification calculated in the first session of day 1 as a reference. The averaged firing rate correlation between sessions with different sensory cues was calculated by using the visual cue session as a reference. In line with the cell selectivity analysis described above, we observed that mid-cue cells active in sessions with different sensory cues displayed significantly lower correlation of firing rates compared to sessions on the same day or across days (left, $\chi^2=27.88$, $p<0.0001$, Kruskal Wallis test). Averaged rate correlations between place cells registered across days were significantly lower than correlations of place cells registered on the same day or in sessions with different sensory cues (left, $\chi^2=18.79$, $p<0.0001$, Kruskal Wallis test). In addition, lap cue cells did not display significant changes in their firing rate correlations between sessions on the same day, across days or with different sensory cues. Taken together, these results indicate that sensory cues are represented by a stable subpopulation of neurons that are highly selective for specific cues while spatial representations undergo major reorganization over several days.

The juxtaposition of inputs from the lateral and medial entorhinal cortex on the dendrites of individual granule cells has been hypothesized to form a conjunctive code for sensory cues and their spatial location (Kesner, 2013; Lee and Jung, 2017). We therefore examined spatial modulation of cue responses by tracking odor cue cells through multiple sessions with different cue-spatial pairing (Figure 2F, G). On average, cue-triggered Ca^{2+} responses were smaller when cues were presented at the infrequent "shift" location within the same session or presented at random locations in a separate session, when compared to the typical responses at the more frequent middle location (Figure 2H, $p<0.0001$, Friedman test, n=101, 5 mice). While we observed a population of bona-fide odor cue cells that displayed similar responses to the odor delivery regardless of cue-spatial pairing (Figure 2G), individual odor cell responses displayed large variability and were often larger in the middle location during normal laps (Figure 2I, S2H). Collectively, these results show that while sensory and spatial representations are generally distinct within the granule cell population, and the same cells tend to respond to the same sensory cue presented at different locations, the firing rate of these cue cells is modulated by the location of that cue in space.

Spatial receptive fields of granule cells are hypothesized to form within a competitive network (de Almeida et al., 2009), in which lateral inhibition mediated by GABAergic interneurons (Espinoza et al., 2018) enforces sparse encoding that may aid pattern separation. The robust and highly selective cue responses of granule cells in our behavioral paradigm allowed us to examine patterns of local-circuit inhibition within the DG network. First, we sought to analyze the effect of cue responses on nonselective background firing observed within the spatially tuned granule cell

bioRxiv preprint doi: https://doi.org/10.1101/2020.02.13.947903; this version posted February 13, 2020. The copyright holder for this preprint (which was not certified by peer review) is the author/funder. All rights reserved. No reuse allowed without permission.

population (n =6,011 cells from 8 mice across 6-9 sessions/mice). By comparing out-of-field firing rates at the middle cue location in laps with cue presentation with laps where the cue is omitted, we identified a significant reduction in background firing of the granule cell population during the cue presentation (Figure 3A, p=0.0004, Signed Rank Sum test). This suppression was absent on cue-omitted laps and generally co-varied with the mean amplitude of cue-related excitation on a session-by-session basis (Figure 3B, R=-0.22, p<0.0001, Signed Rank Sum test). Furthermore, the timing of the peak of this inhibition was delayed with respect to the excitatory cue response in these sessions (Figure S3A, B). These data show that sensory input is able to suppress 'noisy', nonspecific activity in the vicinity of the cue, potentially through lateral inhibition.

In addition to an effect on nonspecific spiking activity in the DG network, we sought to determine the effect of cue responses on activity in the complementary population of place cells and on granule cells responding to other cues. We found that during cue shift laps, firing rates of place cells normally active at the shift location were strongly suppressed (Figure 3D, E). Furthermore when two cues were normally presented at distinct locations, shifting of the position of one cue to the other cue location typically had the effect of suppressing the responses in both cue populations (Figure 3F, G), indicating mutual inhibition among granule cells encoding different cues. This suggests that in addition to inhibition of nonspecific firing, cue responses lead to overall inhibition of place cell responses, and responses to competing cues, as well.

While the most robust form of activity in the DG was found within the cue cell population, the existence of the smaller population of place cells in un-cued locations suggests that spatial activity in these cells is referenced to one of the cues on the otherwise featureless treadmill track in order to encode a unique location. We therefore wanted to determine the effect of manipulations of the variable cue on the subsequent spatial encoding of place cells. For example, if place cells were referenced to the nearest cue we would expect the place fields of cells following the variable middle cue to shift along with this cue on cue shifted laps. To examine the relationship between spatial firing patterns in normal cue laps to those in cue shifted laps, we calculated population vector (PV) correlations of firing rates across all spatially tuned cells in 2 cm bins on each lap (Figure 4A). While the correlation was higher within the vicinity of the cues between normal laps, we observed a dramatic decrease in PV correlation between normal and cue shifted laps which was confined to the location right around the cue itself. Furthermore, effects of cue shifts or omission were largely confined to cells active within a short period around the middle cue (Figure 4B, Figure S4A-C), suggesting that place cells in surrounding locations were not referenced to the variable middle cue. When looking at correlations between spatial firing rates in normal and cue-shifted laps, we found that the majority of cells that shifted their firing to the new cue location were active immediately in response to the cue (Figure 4C). A declining number of cells active at subsequent locations were affected by the shift, rapidly falling below the relatively constant number of place cells unaffected by the shift and therefore referenced to the stable lap boundary cue.

To further evaluate whether cue associated activity contributes to spatial encoding, a spatial Bayesian decoder was constructed from the firing rate vectors of spatially tuned cells (3,093 cells from 60 sessions)(Davidson et al., 2009; Grosmark and Buzsáki, 2016). In order to establish a

bioRxiv preprint doi: https://doi.org/10.1101/2020.02.13.947903; this version posted February 13, 2020. The copyright holder for this preprint (which was not certified by peer review) is the author/funder. All rights reserved. No reuse allowed without permission.

non-biased estimate of the position during treadmill running, the decoding was performed using 5 fold cross validation approach in which the 1/5th of decoded laps were held out from the training set. Post-reconstruction, we divided the data according to the lap types (Figure 4D, Figure S4D, E). The decoder accuracy was higher in normal (median, 10.6 cm) compared to both cue omit (median, 18.4 cm) and cue shift laps (median, 19.6 cm, $\chi 2=32.22$, $p<0.0001$, Kruskal Wallis test, Figure 4E, Figure S4F, G). Notably, the decoder error on shift laps eventually converged to that of normal laps, well before the subsequent lap cue (Figure 4F). Together, these data suggest that the major effects of the variable cue presentation are limited to cells that fire directly in response to the cue, while a majority of place cells are preferentially influenced by the stable cue.

Discussion

By imaging calcium activity in large populations of dentate granule cells during headfixed spatial behaviors, we have shown that the largest population of task-selective neurons is highly sensitive to specific sensory cues rather than to discrete locations (Figure 1). While it is possible that head-restrained linear track behaviors recruit path-integration based navigation to a smaller degree than freely moving experiments, and thus may drive fewer pure place cells, previous experiments have also used similar preparations to ours and found broadly similar results in firing rates and spatial tuning (Aronov and Tank, 2014; Chen et al., 2018). Furthermore, we observed weaker but significant spatial tuning in cells whose receptive fields were displaced from any of the cues present, indicating that animals are indeed able to integrate their motion on the otherwise featureless treadmill belt in order to guide place specific firing. This suggests that cue-selective populations were similarly present in previous experiments recording DG activity *in vivo*, however the lack of precise stimulus control made it impossible to distinguish cue-responsive versus place-responsive components (Leutgeb et al., 2007; Hainmueller and Bartos, 2018; Jung et al., 2019). Indeed, a major impact of sensory cues on DG firing might explain the relatively lower context selectivity and global remapping observed in the DG compared with other hippocampal subfields, at least when measured in different contexts that contain the same or similar sensory cues (Leutgeb et al., 2007; Danielson et al., 2017; GoodSmith et al., 2017; Senzai and Buzsáki, 2017; Hainmueller and Bartos, 2018).

In our experiments, the ability to dynamically manipulate a sensory cue and its association with locations on the treadmill track allowed us to isolate the population of cue-responsive granule cells, in addition to the smaller population of spatially tuned non-cue or “place cells” recorded in the same sessions. Properties of cells within these groups also differed: sensory cue responses were highly-tuned and remarkably robust across locations on the track and over time- significantly more so than the responses of the canonical place cell population (Figure 2A-E). Furthermore, while cue cell responses emerged relatively rapidly during the first exposures to a cue, place cell responses emerged more slowly. This finding suggests that dentate place cells are a more dynamic population than the cue-encoding population, one that gradually adapts to current conditions by integrating between stable cues in order to provide an accurate estimate of the animal’s location at places where no cues are present (Draht et al., 2017).

bioRxiv preprint doi: https://doi.org/10.1101/2020.02.13.947903; this version posted February 13, 2020. The copyright holder for this preprint (which was not certified by peer review) is the author/funder. All rights reserved. No reuse allowed without permission.

Previous work has demonstrated that the two major long range inputs to the dentate, the lateral and medial entorhinal cortex (LEC and MEC), are involved with processing of functionally distinct information (Fyhn et al., 2004; Hargreaves et al., 2005; Wang et al., 2018). This raises the possibility that our "cue cells" may be driven primarily by sensory inputs from the LEC, while "place cells" are driven by self-motion information relayed from the MEC. The segregation of these properties within the overall granule cell population suggests that these streams of information remain largely separated at the level of the DG, similar to the functional heterogeneity observed in other hippocampal subfields (Soltesz and Losonczy, 2018; Cembrowski and Spruston, 2019). This is consistent with current ideas that cue-based and path-integration based navigation are complementary, rather than integrated, in order to produce place-specific firing both in locations where landmark cues are present as well as in between cues (Poucet et al., 2014).

Furthermore, the separation of cue and place responses within the granule cell population suggests that specific inputs from either LEC or MEC dominate individual granule cell firing, which might result from the unique cellular properties of granule cells, local circuits such as inhibitory networks (Pernía-Andrade and Jonas, 2014; Espinoza et al., 2018), as well as the laminated pattern of LEC and MEC inputs onto granule cell dendrites (Witter, 2007). Inputs from distinct cortical afferents can be strongly filtered due to hyperpolarized resting membrane potentials and substantial attenuation of regenerative dendritic activity in granule cells (Krueppel et al., 2011; Kim et al., 2018). Furthermore, short coincidence-detection windows for EPSPs (Schmidt-Hieber et al., 2007) may result in a high activation threshold of each cortical input. Such gating of inputs by postsynaptic neuronal excitability may provide a cellular substrate for our observation that these channels of information remain largely separated at the level of the DG.

But how do these results inform our ideas about how the DG participates in pattern separation and spatial map formation? First, we show that cue responses lead to potent inhibition of three distinct types of granule cell activity: nonspecific "noisy" spiking activity, the spatial firing of place cells normally active in a location, and the activity of cells responsive to other distinct sensory cues (Figure 3). This supports ideas of a competitive network in the DG enforced by strong inhibition, which has been suggested to contribute to pattern separation. In addition, suppression of weaker place cell responses by cue-related activity may indicate that the network is organized to utilize the strongest and perhaps the most informative parameters in order to establish an animal's location in space.

We also found that although the same granule cells respond to similar cues when presented in different locations, the responses were spatially modulated (Figure 2F-I). Differential encoding of cues based upon their spatial location may contribute to pattern separation by differentiating between similar cues at distinct locations. Notably, responses were on average larger for cues presented at a single static location. This suggests that responses are more robust for stimuli paired repeatedly with one particular location, which may indicate dendritic integration of sensory and spatial information, or other factors such as inhibitory plasticity. Conjunctive encoding of sensory cues and their locations within an environment could play a role in establishing landmarks for spatial navigation. In support of this idea, we found that most place cells were referenced to the stable lap cue rather than the variable middle cue, indicating that this cue is preferentially

bioRxiv preprint doi: https://doi.org/10.1101/2020.02.13.947903; this version posted February 13, 2020. The copyright holder for this preprint (which was not certified by peer review) is the author/funder. All rights reserved. No reuse allowed without permission.

utilized as a landmark (Figure 4). Responses were also generally stronger and of higher tuning specificity at the invariant edge cue location than in the variable middle cue location (Figure 1).

Furthermore, rate modulation of granule cell responses to sensory cues resulting from spatial location or association with other cues is a form of "rate remapping", a feature frequently attributed to the dentate gyrus in pattern separation. Thus spatial location, as well as the juxtaposition of multiple cues and their associated patterns of inhibition, may create a rate modulated landscape of granule cell activity specific to the current context. The overall pattern of contextually modulated cue responses in the DG may form the basis for recruitment of distinct populations of neurons, or "global remapping", observed in area CA3. Slower emergence and lower stability over sessions in the place cell population may also point to a role for these neurons in context selectivity.

Together, our findings provide a new perspective on the role of the DG in hippocampal information processing. Our ability to precisely manipulate the presentation of specific sensory cues and their association with locations on the treadmill track has allowed us to unambiguously determine the behavioral parameters to which the dentate population responds, specifically cue or location. These findings help us to better understand the role of the DG in pattern separation and other hippocampal computations that underlie spatial navigation and episodic memory.

Acknowledgements
We would like to thanks the members of the Hen lab for critical insight throughout this project. This work was funded by NIMH T32 MH015144 (S.N.T.), NYSTEM-C029157 (G.O., G.T., C.O.L, R.H.), Revson Senior Fellowship in Biomedical Science (A.D.G.), NIMH R01 AG043688 (R.H.), MH068542 (R.H.), NIMH R01 MH100631 (A.L.), NINDS R01NS094668 (A.L.), and NINDS U19NS104590 (A.L.).

Author Contributions
Conceptualization, C.O.L., S.N.T., and R.H.; Methodology, C.O.L., S.N.T., A.S.; Software, C.O.L., S.N.T., A.D.G., J.B.; Formal Analysis, S.N.T., C.O.L.; Investigation, S.N.T, C.O.L.; Resources, C.O.L., A.D.G., G.T., J.B., A.L., G.O.; Writing, Review and Editing, S.N.T., C.O.L., R.H., A.D.G., A.L.; Supervision, R.H and A.L.

Declaration of Interests
The authors declare no competing interests.

References
de Almeida, L., Idiart, M., and Lisman, J.E. (2009). The input-output transformation of the hippocampal granule cells: from grid cells to place fields. J. Neurosci. *29*, 7504–7512.

Amaral, D.G., Scharfman, H.E., and Lavenex, P. (2007). The dentate gyrus: fundamental neuroanatomical organization (dentate gyrus for dummies). Prog. Brain Res. *163*, 3–22.

Aronov, D., and Tank, D.W. (2014). Engagement of neural circuits underlying 2D spatial navigation in a rodent virtual reality system. Neuron *84*, 442–456.

bioRxiv preprint doi: https://doi.org/10.1101/2020.02.13.947903; this version posted February 13, 2020. The copyright holder for this preprint (which was not certified by peer review) is the author/funder. All rights reserved. No reuse allowed without permission.

Cembrowski, M.S., and Spruston, N. (2019). Heterogeneity within classical cell types is the rule: lessons from hippocampal pyramidal neurons. Nat. Rev. Neurosci. *20*, 193–204.

Chen, G., King, J.A., Lu, Y., Cacucci, F., and Burgess, N. (2018). Spatial cell firing during virtual navigation of open arenas by head-restrained mice. Elife *7*.

Danielson, N.B., Kaifosh, P., Zaremba, J.D., Lovett-Barron, M., Tsai, J., Denny, C.A., Balough, E.M., Goldberg, A.R., Drew, L.J., Hen, R., et al. (2016). Distinct Contribution of Adult-Born Hippocampal Granule Cells to Context Encoding. Neuron *90*, 101–112.

Danielson, N.B., Turi, G.F., Ladow, M., Chavlis, S., Petrantonakis, P.C., Poirazi, P., and Losonczy, A. (2017). In Vivo Imaging of Dentate Gyrus Mossy Cells in Behaving Mice. Neuron *93*, 552-559.e4.

Davidson, T.J., Kloosterman, F., and Wilson, M.A. (2009). Hippocampal replay of extended experience. Neuron *63*, 497–507.

van Dijk, M.T., and Fenton, A.A. (2018). On How the Dentate Gyrus Contributes to Memory Discrimination. Neuron *98*, 832-845.e5.

Draht, F., Zhang, S., Rayan, A., Schönfeld, F., Wiskott, L., and Manahan-Vaughan, D. (2017). Experience-Dependency of Reliance on Local Visual and Idiothetic Cues for Spatial Representations Created in the Absence of Distal Information. Front Behav Neurosci *11*, 92.

Espinoza, C., Guzman, S.J., Zhang, X., and Jonas, P. (2018). Parvalbumin+ interneurons obey unique connectivity rules and establish a powerful lateral-inhibition microcircuit in dentate gyrus. Nat Commun *9*, 4605.

Fuhrmann, F., Justus, D., Sosulina, L., Kaneko, H., Beutel, T., Friedrichs, D., Schoch, S., Schwarz, M.K., Fuhrmann, M., and Remy, S. (2015). Locomotion, Theta Oscillations, and the Speed-Correlated Firing of Hippocampal Neurons Are Controlled by a Medial Septal Glutamatergic Circuit. Neuron *86*, 1253–1264.

Fyhn, M., Molden, S., Witter, M.P., Moser, E.I., and Moser, M.-B. (2004). Spatial representation in the entorhinal cortex. Science *305*, 1258–1264.

Gauthier, J.L., and Tank, D.W. (2018). A Dedicated Population for Reward Coding in the Hippocampus. Neuron *99*, 179-193.e7.

Geiller, T., Fattahi, M., Choi, J.-S., and Royer, S. (2017). Place cells are more strongly tied to landmarks in deep than in superficial CA1. Nat Commun *8*, 14531.

Giovannucci, A., Friedrich, J., Gunn, P., Kalfon, J., Brown, B.L., Koay, S.A., Taxidis, J., Najafi, F., Gauthier, J.L., Zhou, P., et al. (2019). CaImAn an open source tool for scalable calcium imaging data analysis. Elife *8*.

GoodSmith, D., Chen, X., Wang, C., Kim, S.H., Song, H., Burgalossi, A., Christian, K.M., and Knierim, J.J. (2017). Spatial Representations of Granule Cells and Mossy Cells of the Dentate Gyrus. Neuron *93*, 677-690.e5.

bioRxiv preprint doi: https://doi.org/10.1101/2020.02.13.947903; this version posted February 13, 2020. The copyright holder for this preprint (which was not certified by peer review) is the author/funder. All rights reserved. No reuse allowed without permission.

Grosmark, A.D., and Buzsáki, G. (2016). Diversity in neural firing dynamics supports both rigid and learned hippocampal sequences. Science *351*, 1440–1443.

Hainmueller, T., and Bartos, M. (2018). Parallel emergence of stable and dynamic memory engrams in the hippocampus. Nature *558*, 292–296.

Hargreaves, E.L., Rao, G., Lee, I., and Knierim, J.J. (2005). Major dissociation between medial and lateral entorhinal input to dorsal hippocampus. Science *308*, 1792–1794.

Henze, D.A., Urban, N.N., and Barrionuevo, G. (2000). The multifarious hippocampal mossy fiber pathway: a review. Neuroscience *98*, 407–427.

Jung, D., Kim, S., Sariev, A., Sharif, F., Kim, D., and Royer, S. (2019). Dentate granule and mossy cells exhibit distinct spatiotemporal responses to local change in a one-dimensional landscape of visual-tactile cues. Sci Rep *9*, 9545.

Kesner, R.P. (2013). An analysis of the dentate gyrus function. Behavioural Brain Research *254*, 1–7.

Kim, S., Kim, Y., Lee, S.-H., and Ho, W.-K. (2018). Dendritic spikes in hippocampal granule cells are necessary for long-term potentiation at the perforant path synapse. Elife *7*.

Krueppel, R., Remy, S., and Beck, H. (2011). Dendritic integration in hippocampal dentate granule cells. Neuron *71*, 512–528.

Lee, J.W., and Jung, M.W. (2017). Separation or binding? Role of the dentate gyrus in hippocampal mnemonic processing. Neuroscience & Biobehavioral Reviews *75*, 183–194.

Leutgeb, J.K., Leutgeb, S., Moser, M.-B., and Moser, E.I. (2007). Pattern separation in the dentate gyrus and CA3 of the hippocampus. Science *315*, 961–966.

Lisman, J., Buzsáki, G., Eichenbaum, H., Nadel, L., Ranganath, C., and Redish, A.D. (2017). Viewpoints: how the hippocampus contributes to memory, navigation and cognition. Nat. Neurosci. *20*, 1434–1447.

Marr, D., and Brindley, G.S. (1971). Simple memory: a theory for archicortex. Philosophical Transactions of the Royal Society of London. B, Biological Sciences *262*, 23–81.

McNaughton, B.L., Douglas, R.M., and Goddard, G.V. (1978). Synaptic enhancement in fascia dentata: Cooperativity among coactive afferents. Brain Research *157*, 277–293.

O'Keefe, J., and Dostrovsky, J. (1971). The hippocampus as a spatial map. Preliminary evidence from unit activity in the freely-moving rat. Brain Res. *34*, 171–175.

O'Keefe, J., and Nadel, L. (1978). The hippocampus as a cognitive map (Oxford : New York: Clarendon Press ; Oxford University Press).

Pachitariu, M., Stringer, C., Schröder, S., Dipoppa, M., Rossi, L.F., Carandini, M., and Harris, K.D. (2016). Suite2p: beyond 10,000 neurons with standard two-photon microscopy. BioRxiv 061507.

bioRxiv preprint doi: https://doi.org/10.1101/2020.02.13.947903; this version posted February 13, 2020. The copyright holder for this preprint (which was not certified by peer review) is the author/funder. All rights reserved. No reuse allowed without permission.

Pernía-Andrade, A.J., and Jonas, P. (2014). Theta-gamma-modulated synaptic currents in hippocampal granule cells in vivo define a mechanism for network oscillations. Neuron *81*, 140–152.

Pnevmatikakis, E.A., and Giovannucci, A. (2017). NoRMCorre: An online algorithm for piecewise rigid motion correction of calcium imaging data. J. Neurosci. Methods *291*, 83–94.

Poucet, B., Sargolini, F., Song, E.Y., Hangya, B., Fox, S., and Muller, R.U. (2014). Independence of landmark and self-motion-guided navigation: a different role for grid cells. Philos. Trans. R. Soc. Lond., B, Biol. Sci. *369*, 20130370.

Schmidt-Hieber, C., Jonas, P., and Bischofberger, J. (2007). Subthreshold dendritic signal processing and coincidence detection in dentate gyrus granule cells. J. Neurosci. *27*, 8430–8441.

Senzai, Y., and Buzsáki, G. (2017). Physiological Properties and Behavioral Correlates of Hippocampal Granule Cells and Mossy Cells. Neuron *93*, 691-704.e5.

Sheffield, M.E.J., Adoff, M.D., and Dombeck, D.A. (2017). Increased Prevalence of Calcium Transients across the Dendritic Arbor during Place Field Formation. Neuron *96*, 490-504.e5.

Sheintuch, L., Rubin, A., Brande-Eilat, N., Geva, N., Sadeh, N., Pinchasof, O., and Ziv, Y. (2017). Tracking the Same Neurons across Multiple Days in Ca2+ Imaging Data. Cell Rep *21*, 1102–1115.

Skaggs, W.E., McNaughton, B.L., and Gothard, K.M. (1993). An Information-Theoretic Approach to Deciphering the Hippocampal Code. In Advances in Neural Information Processing Systems 5, S.J. Hanson, J.D. Cowan, and C.L. Giles, eds. (Morgan-Kaufmann), pp. 1030–1037.

Soltesz, I., and Losonczy, A. (2018). CA1 pyramidal cell diversity enabling parallel information processing in the hippocampus. Nat. Neurosci. *21*, 484–493.

Treves, A., and Rolls, E.T. (1994). Computational analysis of the role of the hippocampus in memory. Hippocampus *4*, 374–391.

Wang, C., Chen, X., Lee, H., Deshmukh, S.S., Yoganarasimha, D., Savelli, F., and Knierim, J.J. (2018). Egocentric coding of external items in the lateral entorhinal cortex. Science *362*, 945–949.

Witter, M.P. (2007). The perforant path: projections from the entorhinal cortex to the dentate gyrus. Prog. Brain Res. *163*, 43–61.

bioRxiv preprint doi: https://doi.org/10.1101/2020.02.13.947903; this version posted February 13, 2020. The copyright holder for this preprint (which was not certified by peer review) is the author/funder. All rights reserved. No reuse allowed without permission.

Experimental Procedures

Mice

All procedures were conducted in accordance with the U.S. NIH Guide for the Care and Use of Laboratory Animals and the New York State Psychiatric Institute Institutional Animal Care and Use Committees. Adult male C57BL/6J mice were supplied by Jackson Laboratory, and used at 8-10 weeks of age. Mice were housed in a vivarium grouped 2-4 mice/cage enriched with running wheels and maintained on a 12-hour light cycle. Experiments were conducted during the light portion of the cycle. Food and water were available *ad libitum* until the beginning of the experiment, when they were placed under controlled water supply and maintained at >90% of their pre-deprivation weight over the course of imaging experiments. In total, imaging data from 8 mice were used in this study.

Surgery

Dentate gyrus virus injection and imaging window implantation surgeries were performed as described previously (Danielson 2016, 2017). For all surgical procedures, mice were anesthetized with 1.5% isoflurane at an oxygen flow rate of 1 L/min, and head-fixed in a stereotactic frame (Kopf Instruments, Tujunga, CA). Eyes were lubricated with an ophthalmic ointment, and body temperature maintained at 37°C with a warm water recirculator (Stryker, Kalamazoo, MI). The fur was shaved and incision site sterilized prior to beginning surgical procedures, and subcutaneous saline and carpofen were provided peri-operatively and for 3 days post-operatively to prevent dehydration and for analgesia. Mice were unilaterally injected with recombinant adeno-associated virus (rAVV) carrying the GCaMP6s transgene (pAAV.Syn.GCaMP6s.WPRE.SV40) purchased from Addgene (viral prep #100843-AAV1) with titer of 1-5x10^{12} in dorsal dentate gyrus using a Nanoject syringe (Drummond Scientific, Broomall, PA). Injection coordinates were -1.5 mm AP, -2 mm ML, and -1.85, -1.7, -1.55 mm DV relative to the cortical surface. 30 nL of diluted virus was injected at each DV location in 10 nL increments. Mice were allowed to recover for 3 days and then were unilaterally implanted with an imaging window and stainless steel head-post for head fixation. Imaging windows were constructed by adhering 1.8 mm diameter, 2.3 mm long stainless steel hypodermic tubing (Ziggy's Tubes and Wires Inc, Pleasant Hill, TN) to 1.8 mm diameter glass coverslips (Potomac Photonics, Halethorpe, MD). A 1.8 mm diameter craniotomy was made centered on the previous injection site with a taper pointed-drill (Henry Schein Inc, 9004367) and dura was removed with micro curette (FST, 10080-05). The overlying cortex was gently aspirated to reveal capsular fibers with continuous irrigation with ice cold aCSF solution and bleeding was controlled with a collagen gel sponge (Avitene). Under minimal bleeding, a 30g blunt syringe was used to gently aspirate capsular and CA1 alveus fibers with white appearance and CA1 pyramidale and moleculare with pink appearance until vasculature of the hippocampal fissure became visible (under bright light with low bleeding). The cannula, attached to the stereotactic handle, was then gently lowered into the craniotomy and affixed to the skull using dental cement (Unifast Trad powder and LC light cured acrylic UV, Henry Schein).

Behavioral training and apparatus

After a minimum of 1 week recovery period, mice underwent a water restriction scheme (1ml per day) and trained to run on treadmill while head-restrained. The training period typically lasted 7-

bioRxiv preprint doi: https://doi.org/10.1101/2020.02.13.947903; this version posted February 13, 2020. The copyright holder for this preprint (which was not certified by peer review) is the author/funder. All rights reserved. No reuse allowed without permission.

10 days (2 training sessions/day, 15 min each) until the mice were able to run for at least 1 lap/ minute and seek reward from 3 randomly placed reward zones by licking the water delivery port. We then initiated the motorized belt adjusted to the natural velocity of each mouse and proceeded training for 2-3 more days. We did not utilize mice that were not getting all of their daily water supply during treadmill training, and were not motivated to move on the treadmill. A subset of mice preformed treadmill running without the help of motorized belt (Figure S1A).

The behavioral apparatus consisted of 2m long, 3” wide fabric belt stretched between 6” diam. laser-cut plastic wheels, mounted on an aluminum frame (8020.net). Spatial triggering of task events was performed by custom software via serial communication with a microcontroller (Arduino DUE) and an associated circuit board (OpenMaze OM4 PCB, www.openmaze.org) on the treadmill. The axle of the treadmill wheel was attached to a quadrature rotary encoder (US Digital part #: MA3-A10-125-B) connected to a custom quadrature decoder board and Arduino Nano (courtesy of Wen Li). Angular displacement was converted into a virtual linear distance based on the circumference of the treadmill. The errors were corrected via a registration anchor marked by radio-frequency identification (RFID) buttons (SparkFun Electronics) at the lap boundary of the belt and was detected when it passed over an RFID reader (ID-12LA, SparkFun) affixed underneath the mouse. A 12V DC gear motor was attached to the axle of the treadmill connected to a separate Arduino/OpenMaze shield using pulse-width modulation to adjust the rotation speed. A water reservoir connected to a water delivery port consisting of a small gavage needle (Cadence Science) was placed within reach of the mouse’s tongue. A capacitance touch sensor (Sparkfun #MPR121) was attached to the water port to measure licking and the sensor was connected to the Arduino/OM4 PCB. Small 2-3ml drops of water were delivered by the brief opening a solenoid valve (Parker Hannefin) connected to the water port. Rewards were triggered at random locations each lap when mice entered a 10cm long reward zone on the track and were available until mice exited the reward zone or 3 sec had elapsed. Olfactory stimuli consisted of undiluted isoamyl acetate (IAA, Sigma W205532) which was added to syringe filters (Whatman #6888-2527) and delivered by opening a solenoid valve (SMC) connected to a flow controller delivering constant airflow of compressed medical grade air for 1s (~3psi). Visual and tactile stimulation consisted of a red LED contralateral to the imaged region, or a 1” square piece of sand paper brushed by the contralateral whiskers using a stepper motor, at approximately the speed of the treadmill belt. Custom written B-Mate algorithm implemented in Java was used for recording mice’s licking, its position on the belt, and cue delivery. Mice were monitored using an IR camera (PS3eye) and illuminated using an IR LED array.

To isolate cue-selective responses among the granule cell population, normal cue laps in which the olfactory, visual, or tactile cue was presented in the middle of the treadmill track (90-110cm) were interspersed with occasional laps in which the same cue was omitted (“omit” laps), or shifted forward ¼ of the track (“shift” laps). For a subset of sessions, the olfactory cue was presented at one of 5 locations along the track randomly each lap, in order to examine the effect of spatial pairing of the cue. In all experiments, the treadmill belt was changed between sessions to reduce the chances of urine contamination which might act as an additional olfactory cue.

bioRxiv preprint doi: https://doi.org/10.1101/2020.02.13.947903; this version posted February 13, 2020. The copyright holder for this preprint (which was not certified by peer review) is the author/funder. All rights reserved. No reuse allowed without permission.

In vivo two-photon imaging

Imaging was conducted using a microscope setup which consists of 8kHz resonant galvanometer (*Bruker*) mounted to a mirror-based multi-photon microscopy system (*Prairie Technologies*) and an ultra-fast pulsed laser beam (920-nm wavelength; *Chameleon Ultra II, Coherent*, 20–40-mW average power at the back focal plane of the objective) controlled with an electro-optical modulator (*Conoptics*, Model 302 RM). GCaMP fluorescence was excited through a 40x water immersion objective (Nikon NIR Apo, 0.8 NA, 3.5 mm WD) and fluorescence signals detected with photomultiplier tubes (*Hamamatsu 7422P-40*), acquired with PrairieView software (*Prairie*) at 30fps frame rate (512X512 pixels, 1.3 mm/pixel). A custom dual stage preamp ($1.4X10^5$ dB, Bruker) was used to amplify signals prior to digitization. Two goniometers (Edmund Optics) were used to adjust the angle of each mouse's head in order to achieve the same imaging plane over multiple sessions.

Data processing for Ca^{2+} imaging. Movies were motion corrected using NoRMCorre algorithm using a non-rigid registration method that splits the field of view (FOV) into overlapping patched that are registered separately then merged by smooth interpolation (Pnevmatikakis and Giovannucci, 2017). Videos were then spatially and temporally down-sampled by a binning factors of 2 and 2 to reduce noise and the computational power required for cell segmentation. Spatial and temporal components for individual cells were extracted using large-scale sparse non-negative matrix factorization (Giovannucci et al., 2019) or using the singular value decomposition method by Suite2p algorithm (https://github.com/cortex-lab/Suite2P), both of which resulted in similar number of regions of interest (ROIs). We used Suite2p graphical user interface to manually select small, densely packed DG granule cells and discard large isolated cell bodies corresponding to mossy cells or other hilar interneurons. Ca^{2+} transient events were defined by a custom detection algorithm which identifies fluorescence peaks with a rise slope greater than 4 standard deviations above an iteratively refined baseline.

Behavioral and Calcium Data Alignment. Behavioral data was aligned to Ca^{2+}data using the record of a synchronization signal between the two computers used for data collection. Behavioral data was down-sampled to match Ca^{2+} imaging data.

Data Analysis

Data were analyzed using custom-written routines implemented in MATLAB. Plots were generated in MATLAB and Prism and edited in Adobe Illustrator CC 2018.

Identification of spatially-tuned neurons. We restricted our analysis to continuous running at least 2 sec in duration and with a minimum peak speed of 5 cm/sec. For each lap crossing, position data and Ca^{2+} transient events for each cell were binned into 2 cm-wide windows (100 bins), generating raw vectors for occupancy-by-position and transient numbers-by-position which were then circularly smoothed with a Gaussian kernel ($SD = 5$ cm). A firing rate-by-position vector was computed by dividing the smoothed transient number vector by the smoothed occupancy vector. Within each lap, we circularly shuffled the positions 1000 times and recomputed firing rate-by-position vectors to generate a null distribution for each spatial bin. A spatially selective cell was defined that met the following criteria: (a) the cell should fire above its mean firing rate within its

bioRxiv preprint doi: https://doi.org/10.1101/2020.02.13.947903; this version posted February 13, 2020. The copyright holder for this preprint (which was not certified by peer review) is the author/funder. All rights reserved. No reuse allowed without permission.

spatial field in at least 20% of laps or for a minimum of 3 laps; and (b) observed firing should be above 99% of the shuffled distribution for at least 5 consecutive spatial bins (10 cm) wrapping around the two edges of the belt. We have identified spatially tuned neurons by excluding bins in which sensory cues were omitted or shifted and calculated firing rate vectors in these laps separately. Among all of the spatially tuned neurons, "middle cue cells" were defined as those with averaged spatial fields that overlapped with at least 50% of the 45th and 55th bins and had peak amplitude at least two times larger than those in cue-omitted laps and cue shifted laps. "Lap-cue cells" were defined as those with averaged spatial fields overlapping at least 50% of the region wrapping around the 90th and 10th bins in the normal laps and have peak amplitude in cue-omitted laps and cue shifted laps not exceeding than at least two times of that in normal laps. The remaining cells constituted the "place cells".

Spatial information, stability, consistency, and emergence of spatial fields. To calculate a measure for spatial information content for granule cells in Figure 1, we adapted a traditional method of spatial information assessment (Danielson et al., 2016; Skaggs et al., 1993) to Ca^{2+} imaging data. For each cell, we used the firing rate-by-position vector and shuffled null distribution computed above and calculated the spatial information content for each as described previously (Skaggs et al., 1993). To account for the low firing rates artificially producing high spatial information scores, we subtracted the mean of the shuffled information per spike from observed information per spike, divided by the standard deviation of the shuffled values to determine the spatial variance for each cell. Therefore, the amount of spatial information is inferred from differences in normalized Ca^{2+} activity in each neuron and reported as bits per s. To measure spatial field correlation across environments in Figure S1, after identifying spatially tuned neurons, we calculated a Pearson's correlation coefficient between a cell's averaged firing rate-by-position vector in different sessions. The consistency of place field firing was determined as the cross-correlation between the averaged firing rate-by-position vector of the first and the second halves of the total number of cue normal laps within a session. We determined place field onset lap in cue normal laps (Figure 1) as described previously (Sheffield et al., 2017). Briefly, starting on lap 1 we searched for a significant Ca^{2+} transient event present within the boundaries of the previously determined mean spatial field calculated from all the laps in the session. If one were found we would then search for Ca^{2+} transient event on each of the next 4 laps. If 3 of the 5 laps had Ca^{2+} transients within the mean place field boundaries, lap 1 would be considered the place field onset lap. If either lap 1 had no Ca^{2+} transient or less than 3 of the 5 laps had Ca^{2+} transient, we would move to lap 2 and repeat the search. To determine place field onset lap in cue shifted laps (Figure 1), we searched for the first Ca^{2+} transient event on 2 of 4 consecutive cue shifted laps.

Multi-Session Cell Tracking. Cells were tracked across sessions using CellReg (Sheintuch et al., 2017). Briefly, rigid alignment with both translations and rotations was performed on spatial footprint projections of each session and manually inspected for quality. To improve performance with our data, we modified the CellReg source code to consider complete spatial footprints instead of centroids during alignment. The centroid distance between neighbors was then calculated and used to create a probabilistic model that estimated the expected error rate at different thresholds. The optimal centroid distance threshold was chosen by the algorithm and used to match cells. A clustering algorithm then refined these decisions previously made using pairwise comparisons.

bioRxiv preprint doi: https://doi.org/10.1101/2020.02.13.947903; this version posted February 13, 2020. The copyright holder for this preprint (which was not certified by peer review) is the author/funder. All rights reserved. No reuse allowed without permission.

Following cell registration, tracked cells were matched with their corresponding functional cell types (i.e. mid-, lap-cue, place cells, as described above). All analyses presented in Figure 2 are carried out in pairwise, to maximize the number of cells in each comparison and to minimize the total number of comparisons. For multiday comparisons we used Day1, session 1 as the normal session, and for multisession comparisons we used Visual stimulus session as the normal session. To calculate the fraction of cells that maintain their identity, cell pairs that were counted as being the same cell type in both sessions was divided by all of that cell type in the normal session. In order to derive a null distribution for preservation of pairwise identity, we randomly permutated the cell IDs of all the tracked cells in pairwise sessions 1000 times and calculated the fraction of cells that were the same, among all of that cell type in the normal session. We calculated p-values by comparing actual data to this null distribution, 97.5th% of the null distribution is presented dotted lines in Figure 2.

Population vector (PV) and rate correlation analysis. The variability in neural activity between lap types was calculated by using Pearson's correlation on each 2 cm bins of the firing rate-by-position vector along the treadmill during odor cue trials (mean for all spatially tuned cells). Comparison of the activity between different sessions was calculated using Pearson's correlation of the spatially binned, averaged firing rate-by-position vector in cue normal laps of all recorded cells in 8 mice for multiday analysis (1 session from each condition) and 6 mice for multisession analysis (1 session from each condition) in Figure 2.

Inhibition analysis

Out-of-field firing was calculated for cells found to be significantly spatially tuned on normal middle cue laps by extracting calcium event rates in the ~200cm track length excluding the peak place field (+/- 10cm). Average out-of-field firing rates were then calculated across all cells for cue laps and intermittent laps where the cue was omitted. For comparison of cue-associated excitation and inhibition levels, average firing rates were computed by session for the 20cm region surrounding the middle cue, with respect to the normal pre-cue baseline firing rate. Cue-related inhibition of place cell firing was calculated by selecting spatially tuned cells whose firing field on normal middle cue laps fell within the region of the cue on shift laps (50-80cm). Firing rates for these cells were then averaged for normal laps where the cue was not presented in this region and compared with laps where the cue was shifted to this region (50cm). Mutual inhibition between cues was calculated by first selecting cells responsive to each of 2 cues of different modalities (olfactory or visual) presented at 40cm and 120cm. Responses were then averaged for each cue cell for laps in which the cues were presented alone at these locations versus intermittent laps where the cues were presented together at one of the two former locations.

Cue shift analysis

Spatial firing rates for each spatially tuned cell on normal middle cue laps were cross-correlated with firing rates on shift laps in order to estimate the shift magnitude for each cell after cue manipulation. Binned histograms of numbers of cells with peak firing rates at particular locations along the track were plotted with respect to their shift magnitudes. Numbers of cells were

bioRxiv preprint doi: https://doi.org/10.1101/2020.02.13.947903; this version posted February 13, 2020. The copyright holder for this preprint (which was not certified by peer review) is the author/funder. All rights reserved. No reuse allowed without permission.

averaged over populations showing no shift (-5 to 5 cm shift) or that shifted their firing along with the cue (25cm +/-5cm).

Bayesian Reconstruction Analysis. To calculate the probability of the animal's position given a short time window of neural activity, we used a previously published method based on Bayesian reconstruction algorithm(Davidson et al., 2009; Grosmark and Buzsáki, 2016). Briefly, Ca^{2+} transient events for each cell were binned into 1 second windows to construct firing rate vectors. For each of these binned firing rate vectors, Bayesian classification of virtual position (posterior probability for each bin) was performed by a previously described method (Grosmark and Buzsáki, 2016) utilizing a template comprising of a cell's smoothed firing rate-by-position vectors. In order to cross-validate our decoding procedure, we divided firing rate-by-position template into lap crossings, used $1/5^{th}$ of laps as "testing" dataset while the remaining $4/5^{th}$ of laps constituted the "training" dataset. For example, lap 1 was tested based on the firing rate-by-position vectors calculated using laps 2,3,4,5, lap as template, and lap 6 was tested based on the firing rate-by-position vectors calculated from laps 7,8,9,10, and so on. The resulting posterior probability distribution for each bin is the likelihood for an animal is located in that bin, which adds up to 1, and the bin with the maximum posterior probability is the estimated position of the animal. To determine the decoding error we calculated the absolute difference between the animal's actual position and the maximum posterior probability in that bin. Post-reconstruction, we divided the time bins (excluding those with no activity) according to the lap types.

Data and Software Availability

Data and custom programs are available upon reasonable request.

bioRxiv preprint doi: https://doi.org/10.1101/2020.02.13.947903; this version posted February 13, 2020. The copyright holder for this preprint (which was not certified by peer review) is the author/funder. All rights reserved. No reuse allowed without permission.

Figure 1 Representation of sensory cues and place in the dentate gyrus

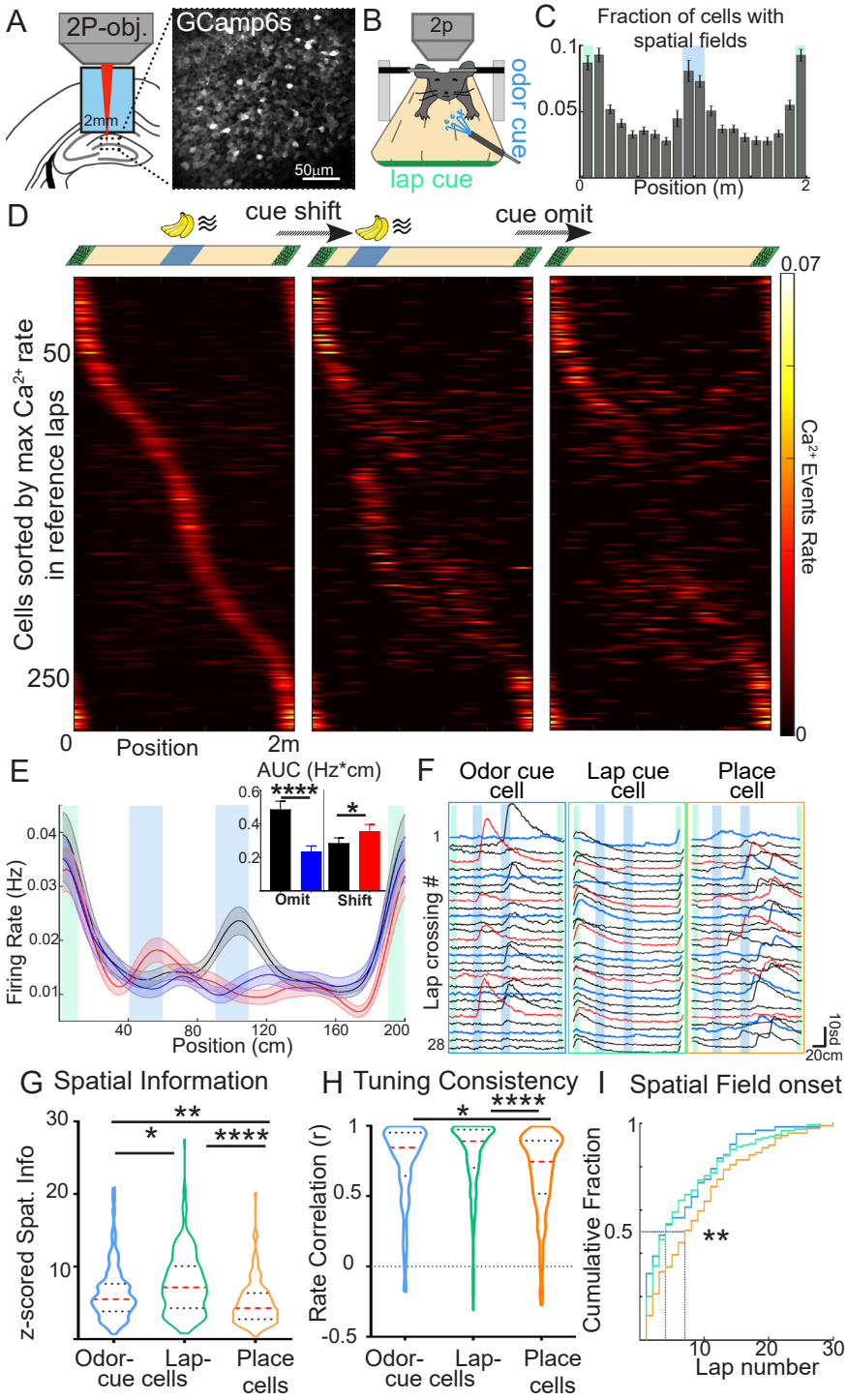

bioRxiv preprint doi: https://doi.org/10.1101/2020.02.13.947903; this version posted February 13, 2020. The copyright holder for this preprint (which was not certified by peer review) is the author/funder. All rights reserved. No reuse allowed without permission.

Figure 2. Stability and specificity of sensory cue representations

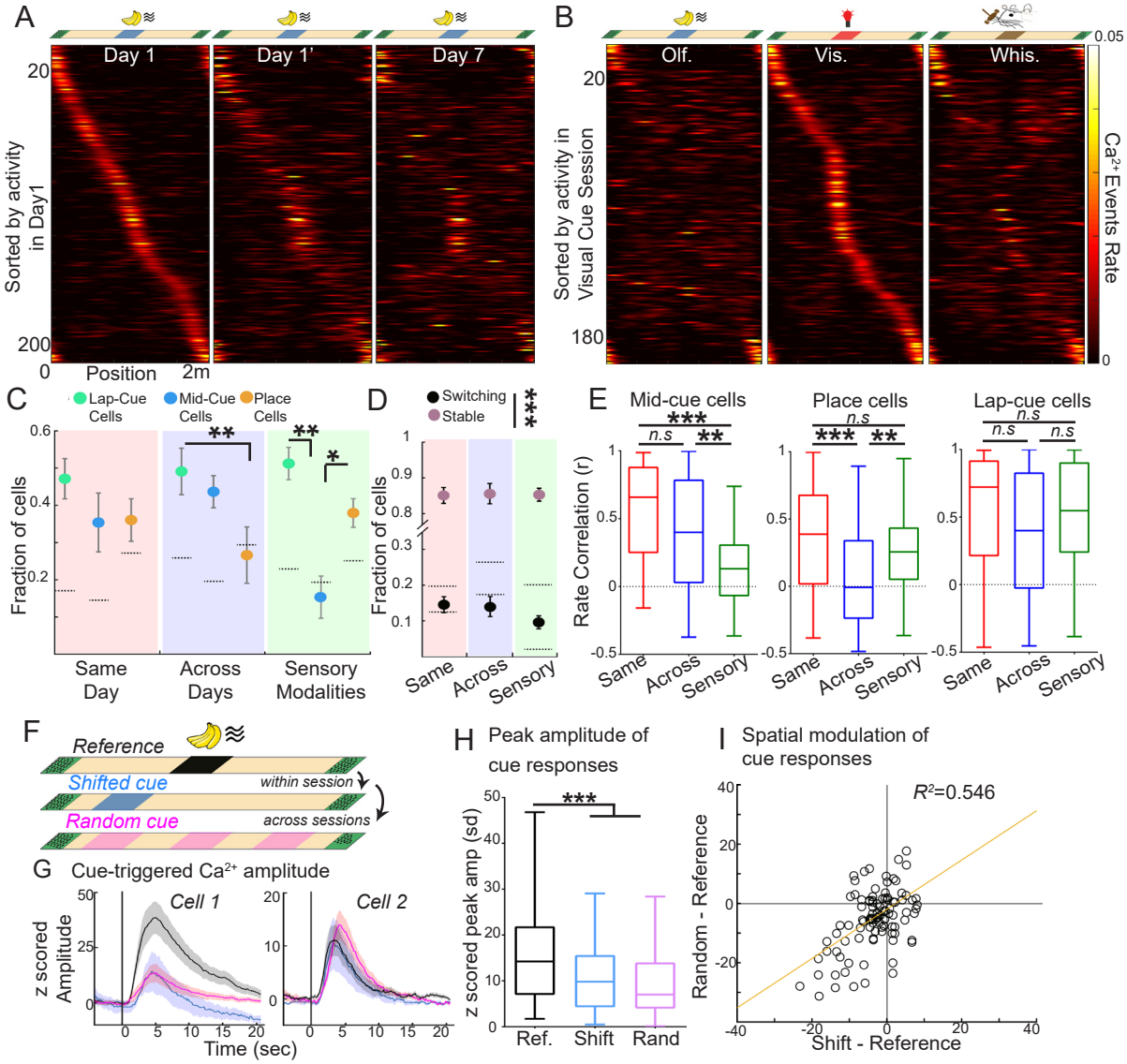

bioRxiv preprint doi: https://doi.org/10.1101/2020.02.13.947903; this version posted February 13, 2020. The copyright holder for this preprint (which was not certified by peer review) is the author/funder. All rights reserved. No reuse allowed without permission.

Figure 3: Suppression of diverse types of DG responses during cue presentation

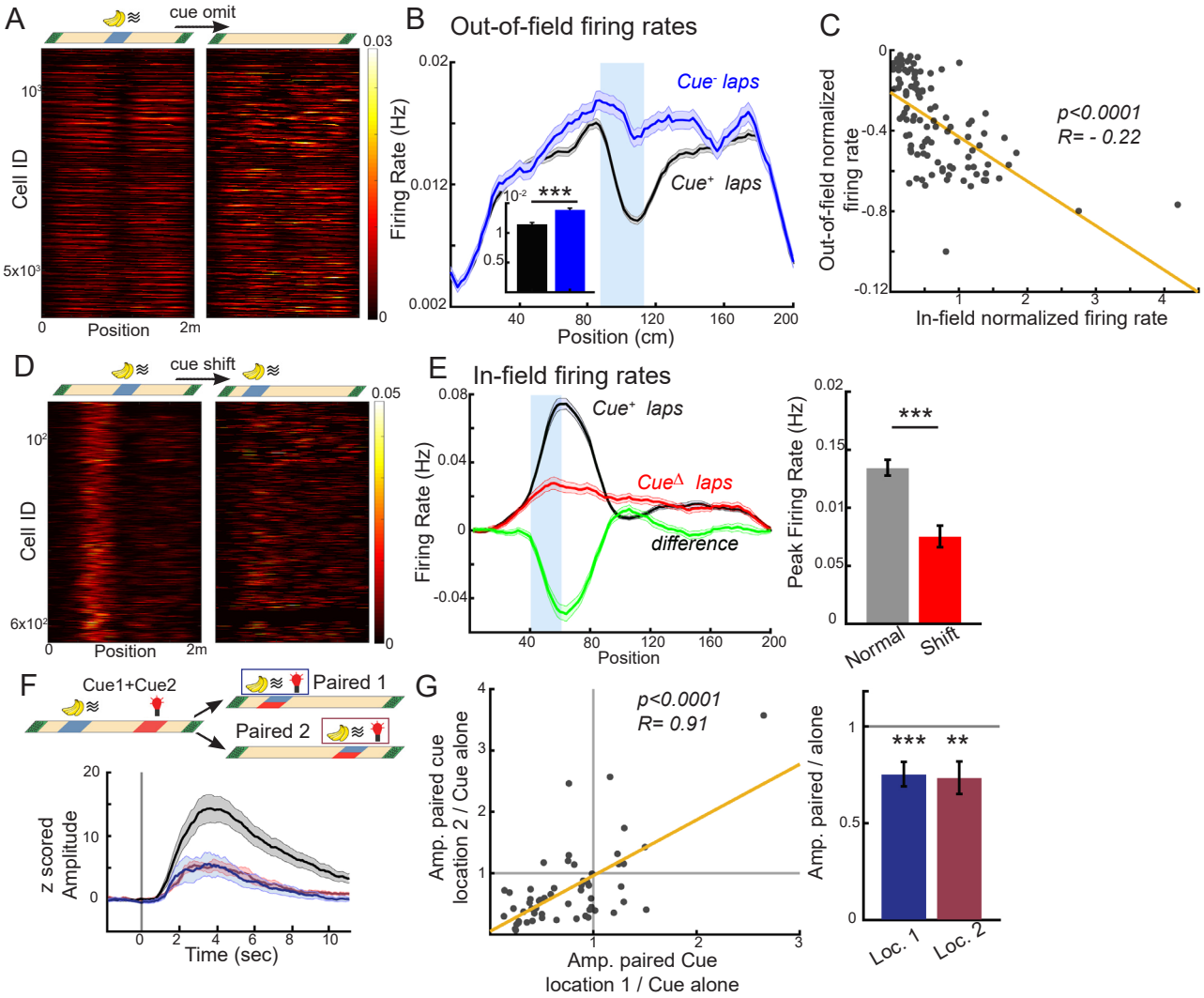

bioRxiv preprint doi: https://doi.org/10.1101/2020.02.13.947903; this version posted February 13, 2020. The copyright holder for this preprint (which was not certified by peer review) is the author/funder. All rights reserved. No reuse allowed without permission.

Figure 4. Contribution of cue associated activity to population activity

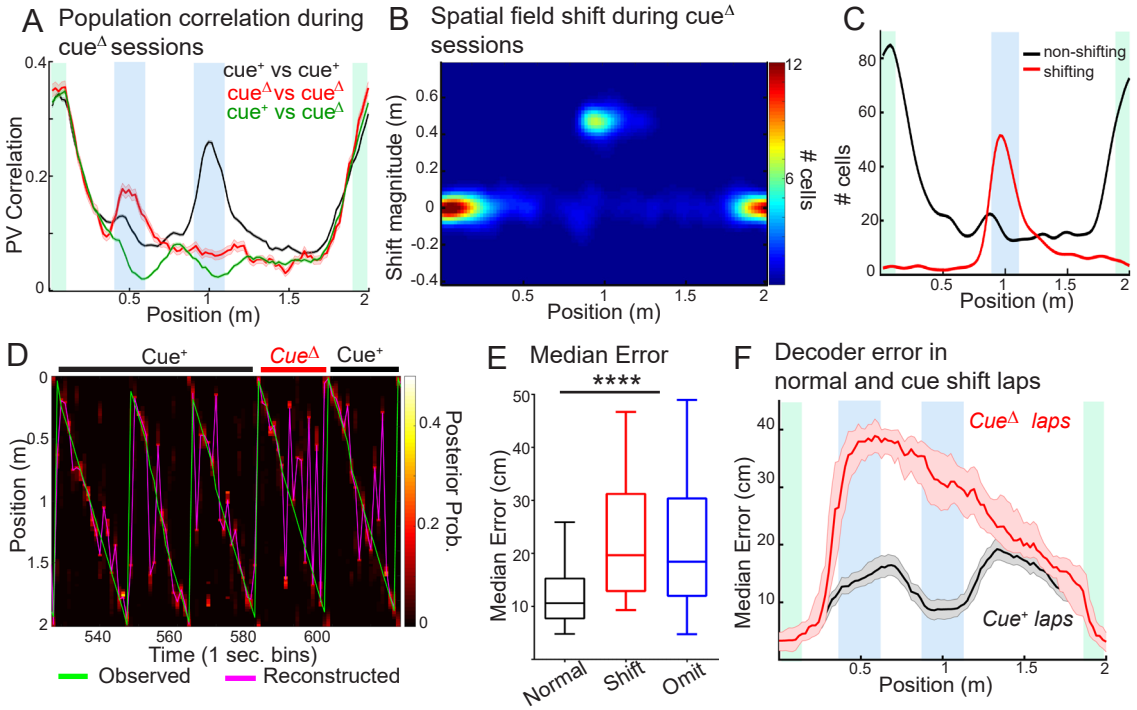

Figure S1: Representation of sensory cues and place in the DG

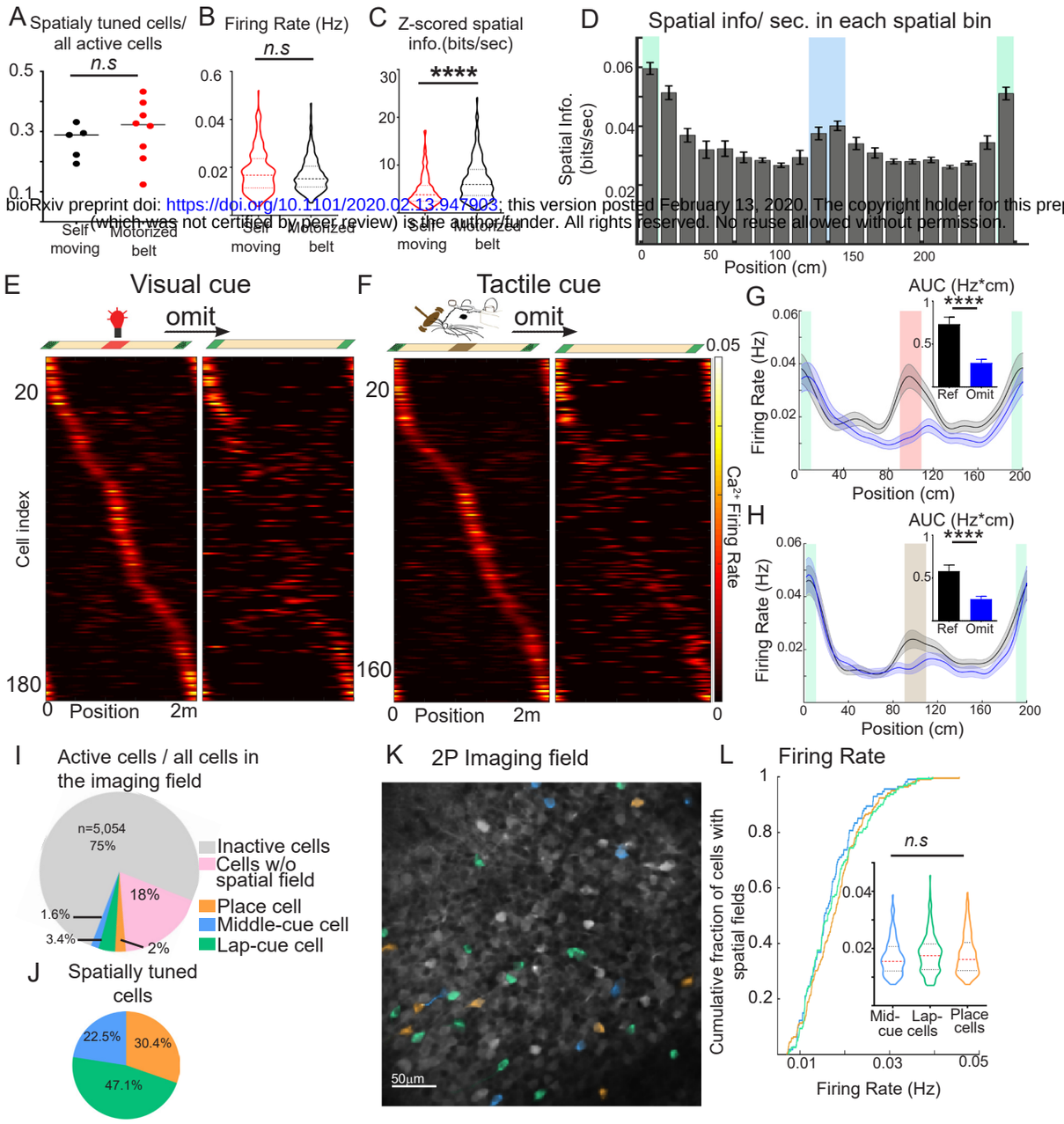

bioRxiv preprint doi: https://doi.org/10.1101/2020.02.13.947903; this version posted February 13, 2020. The copyright holder for this preprint (which was not certified by peer review) is the author/funder. All rights reserved. No reuse allowed without permission.

bioRxiv preprint doi: https://doi.org/10.1101/2020.02.13.947903; this version posted February 13, 2020. The copyright holder for this preprint (which was not certified by peer review) is the author/funder. All rights reserved. No reuse allowed without permission.

Figure S2. Multisession tracking of single cue and place cells

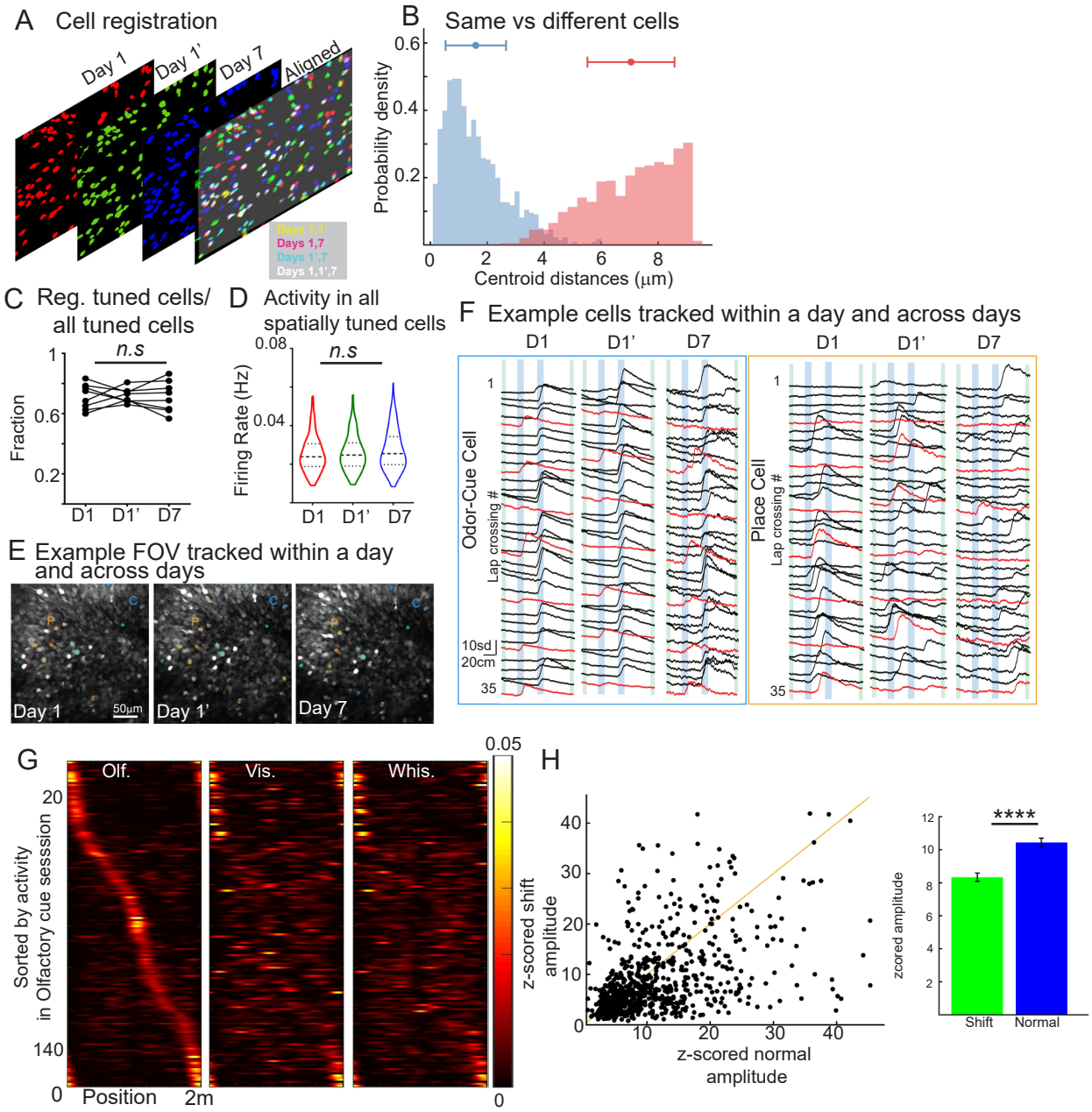

bioRxiv preprint doi: https://doi.org/10.1101/2020.02.13.947903; this version posted February 13, 2020. The copyright holder for this preprint (which was not certified by peer review) is the author/funder. All rights reserved. No reuse allowed without permission.

Figure S3: Cue-associated inhibition

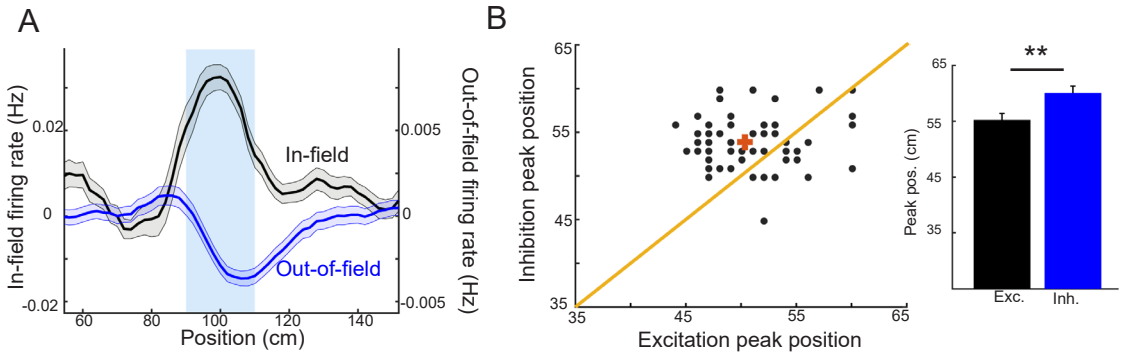

bioRxiv preprint doi: https://doi.org/10.1101/2020.02.13.947903; this version posted February 13, 2020. The copyright holder for this preprint (which was not certified by peer review) is the author/funder. All rights reserved. No reuse allowed without permission.

Figure S4. Spatial limits of cue effects

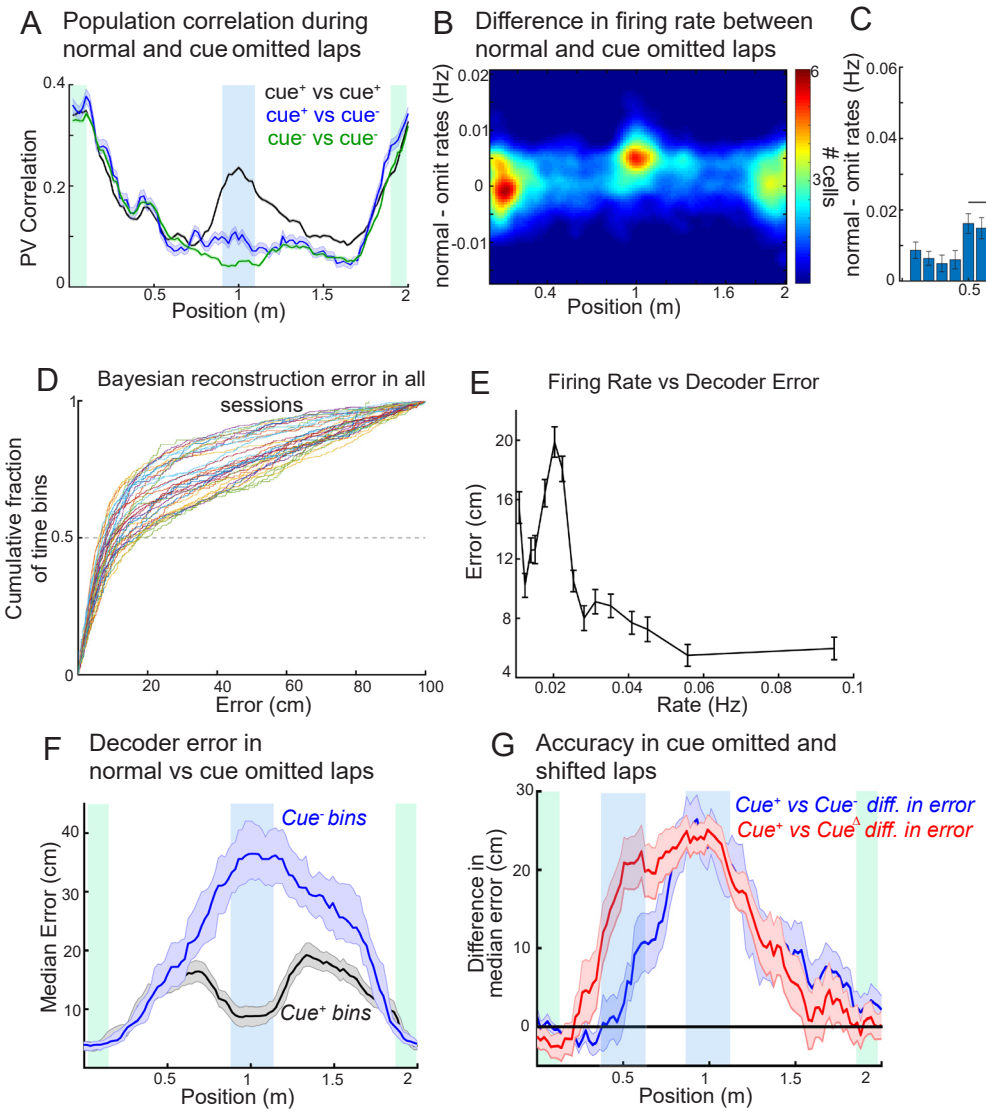

bioRxiv preprint doi: https://doi.org/10.1101/2020.02.13.947903; this version posted February 13, 2020. The copyright holder for this preprint (which was not certified by peer review) is the author/funder. All rights reserved. No reuse allowed without permission.

Figure Titles and Legends

Figure1: Representation of sensory cues and place in the dentate gyrus

A) Two-photon imaging of DG population calcium activity. Left, diagram of the imaging window implant in the dorsal dentate gyrus. Right, Time averaged in vivo two-photon image of GCaMp6s-expressing granule cells.

B) Diagram of head-fixed treadmill apparatus for spatial sensory cue delivery.

C) Fraction of spatially tuned cells at each linearized treadmill position (bins=10cm) per session, n = 5,011 cells from 8 mice across 6-9 sessions/mouse, locations of the odor and lap cue are shown blue and green shaded areas, respectively.

D) Spatial patterns of DG neuron activity during cue task. Top: Location of lap cue (green boxes) and an odor cue (blue box), on normal, shift or omit laps. Bottom: spatial firing rates of 285 spatially tuned neurons (n=8 mice) during their first exposure to the middle cue on normal (left), cue-shifted (middle) and cue-omitted (right) laps. Each row represents a cell, and the x axis represents the treadmill position.

E) Average firing rates by position of neurons shown in panel D on normal (black), cue-shifted (red) and cue-omitted laps (blue, mean ± SEM). (Inset) averaged area under the firing rate curves (Hz*cm) within the middle cue region during normal (black bar), cue omitted (blue bar), and cue shifted laps (red bar). $P_{normal\text{-}omit}$ <0.0001, $P_{normal\text{-}shift}$ =0.02, Wilcoxon matched-pairs signed rank test, error bars are mean ± SEM.

F) Example fluorescence traces from odor-cue, lap-cue and place cells within a single session. Black, red, and blue traces represent normal, cue shifted and omitted laps, respectively. Scale bars are cm and standard deviation from each cell's baseline fluorescence.

G) Z scored spatial information of cue and place cell populations. Z scored spatial information, χ^2=48.47, p<0.0001, $P_{OdorCue\text{-}LapCue}$=0.0387, $P_{OdorCue\text{-}Place}$=0.0028, $P_{LapCue\text{-}Place}$<0.0001.

H) Tuning consistency of cue and place cells. Firing rate correlation between first and last halves of the session, χ^2=32.60, p<0.0001, $P_{OdorCue\text{-}LapCue}$=0.2224, $P_{OdorCue\text{-}Place}$=0.0117, $P_{LapCue\text{-}Place}$<0.0001.

I) Emergence of cue and place responses. Cumulative distribution of spatial field onset lap in normal laps for cue and place cells, χ^2=9.29, p=0.0096, $P_{OdorCue\text{-}LapCue}$=0.8925, $P_{OdorCue\text{-}Place}$=0.0194, $P_{LapCue\text{-}Place}$=0.0091.

$N_{OdorCue}$=114, N_{LapCue}=220, $N_{PlaceCell}$=160, from 8 mice 2 sessions each. Red dotted lines in violin plots show median, black dotted lines show quartiles. Comparisons are Kruskal Wallis and Dunn's multiple comparisons tests. *P < 0.05; **P < 0.01; ***P < 0.001. See also Fig. S1.

Figure 2: Stability and selectivity of sensory cue and place responses

A) Spatial firing rates of individual DG neurons matched between sessions and days. Top: diagram of odor cue presentation on different sessions within same day or 1wk later. Bottom: Spatial firing rates for tracked neurons during two subsequent sessions in day1 or one week later are ordered according to the position of peak activity during the first exposure to the treadmill. Data is shown for GCs with significant tuning in day1 session1 and registered in the next session of the same day and 1 week later (n=233 cells, 8 mice).

B) Activity of DG neurons in response to different sensory cues. Top: diagram of imaging during exposures to cues of different sensory modalities in the middle position and an invariant lap cue

bioRxiv preprint doi: https://doi.org/10.1101/2020.02.13.947903; this version posted February 13, 2020. The copyright holder for this preprint (which was not certified by peer review) is the author/funder. All rights reserved. No reuse allowed without permission.

(See also Fig S1E-H). Bottom: Spatial tuning for tracked neurons in consecutive sessions during exposures to different cues. Data is shown for neurons with significant tuning in visual cue session and tracked in olfactory and whisker tactile cue sessions (n=196 cells, 6 mice).

C) Fraction of cells that encoded the same variable, lap cue (green), middle cue (blue), or place (orange), within same day (left), across days (middle), and during exposures to different sensory modalities (right) . Cells encoding the same variable on the same day, χ^2=1.81, p=0.4039, $P_{LapCue-OdorCue}$=0.4221, $P_{LapCue-Place}$=0.549, $P_{OdorCue-Place}$=0.9713; cells encoding the same variable across days, χ^2=14.36, p<0.001, $P_{LapCue-OdorCue}$=0.1566, $P_{LapCue-Place}$<0.0001, $P_{OdorCue-Place}$=0.0313 (8 mice, 8 matched sessions, Day1-Day1', Day1-Day7); cells encoding the same variable with different sensory modalities, χ^2=19.78, p<0.00001, $P_{LapCue-OdorCue}$<0.00001, $P_{LapCue-Place}$=0.0766, $P_{OdorCue-Place}$=0.0464 (6 mice, 12 matched sessions, Odor-Vis. and Vis.-Tact.); Kruskal-Wallis test, Dunn's multiple comparisons test. Dashed lines represent 97.5th% of null distributions for each cell type. Error bars, mean ± SEM.

D) Fractions of spatially tuned cells that stably encoded only one variable (cue or place, pink) or switched response types (cue to place or vice versa, black) within same day, across days and in response to different sensory cues: $P_{Switch-Stable\ (Same\ Day)}$<0.001, $P_{Switch-Stable\ (Across\ Days)}$<0.001, $P_{Switch-Stable\ (Sensory\ Modalities)}$<0.001, Wilcoxon Rank Sum test. Dashed lines: 2.5th and 97.5th% of null distributions. Error bars, mean ± SEM.

E) Mean rate correlations within the same day (red), different days (blue) and different sensory cues (green) for mid-cue cells (left, χ^2=27.88, p<0.0001, $P_{Same\ Day-Across\ Days}$=0.2465, $P_{Same\ Day-Sensory\ Modalities}$<0.0001, $P_{Across\ Days-Sensory\ Modalities}$=0.0038, $N_{Same\ Day}$=37, $N_{Across\ Days}$=37, $N_{Sensory\ Modalities}$=55); place cells (middle, χ^2=18.79, p<0.0001, $P_{Same\ Day-Across\ Days}$<0.0001, $P_{Same\ Day-Sensory\ Modalities}$=0.7449, $P_{Across\ Days-Sensory\ Modalities}$=0.0055, $N_{Same\ Day}$=76, $N_{Across\ Days}$=76, $N_{Sensory\ Modalities}$=83), lap-cue cells (right, χ^2=5.096, p=0.0782, $P_{Same\ Day-Across\ Days}$=0.0723, $P_{Same\ Day-Sensory\ Modalities}$>0.9999, $P_{Across\ Days-Sensory\ Modalities}$=0.7932, $N_{Same\ Day}$=80, $N_{Across\ Days}$=80, $N_{Sensory\ Modalities}$=59). Kruskal-Wallis test, Dunn's multiple comparisons test. Boxes, 25th to 75th percentiles; bars, median; whiskers, 99% range.

F) Spatial modulation of cue responses. Olfactory cue cells are selected by activity in cue-shift sessions and matched to cells found in random-cue sessions. Cue-triggered responses are averaged for middle cue, cue-shift, and random cue conditions.

G) Example cue triggered average Ca^{2+} transients of two cue cells on normal (black), cue-shifted (blue) and random-cue (pink) laps. Scale bars are sec and standard deviation from each cell's baseline fluorescence.

H) Z-scored peak amplitudes of Ca^{2+} transients of odor cue cells in normal, shift and random cue presentation conditions; χ^2=49.36, p<0.001, $P_{Normal-Shift}$<0.0001, $P_{Normal-Random}$<0.0001, $P_{Shift-Random}$>0.9999, Friedman test and Dunn's multiple comparisons tests (n=101 cells, 5 mice). Boxes, 25th to 75th percentiles; bars, median; whiskers, 99% range.

I) Difference of magnitude of cue responses in random-cue from normal laps vs. the difference of responses in cue-shift from normal laps. Yellow line represents linear regression line, R^2= 0.546).

**P* < 0.05; ***P* < 0.01; ****P*< 0.001. See also Fig. S2.

bioRxiv preprint doi: https://doi.org/10.1101/2020.02.13.947903; this version posted February 13, 2020. The copyright holder for this preprint (which was not certified by peer review) is the author/funder. All rights reserved. No reuse allowed without permission.

Figure3: Suppression of diverse types of DG responses during cue presentation

A) Cue-related suppression of out-of-field firing. Spatial firing rates outside of the field center-of-mass (+/-10cm) for significantly tuned cells during normal and cue omitted laps.

B) Average out of field firing rates of spatially tuned cells in the presence of cue (black) compared to laps in which cue is omitted (blue). Blue shaded area shows the cue delivery position. Inset, mean ± SEM of firing rate, $p<0.001$, rank-sum test, n=6,011 cells.

C) Correlation between cue-related excitation and inhibition. Session averaged in-field firing rate vs. out-of-field firing rate (76 sessions). Yellow, linear regression: $p<0.0001$, $R^2=-0.22$.

D) Cue-related suppression of place cell firing. Spatial firing rates of place cells with firing fields at 40-80cm during normal laps and laps in which the cue is shifted to 40cm.

E) (Left) Average firing rate by position for the above place cells in normal laps when the cue is not presented at this location (black), compared with laps in which the cue is shifted to this location (shift, cue(delta) laps, red; difference in green). (Right), Average peak firing rate of the same cells in D and E, paired t-test, $p<0.001$, 645 cells.

F) Cue-related suppression of cells responding to other cues. Top, diagram of intermittent cue pairing experiment. Cues of two different modalities were presented at different locations, interspersed with paired presentation of these two cues at one of these locations. Bottom, example cue-triggered averaged Ca^{2+} transients for a cue cell strongly active when the cue is presented alone (black) but reduced responses when paired with a different cue, regardless of location (blue, location #1, purple, location #2).

G) (Left) Amplitudes of paired cue responses at two pairing locations with respect to the response to the cue alone. Yellow line represents the linear regression line, $p<0.0001$, $R^2=0.91$, n=56 cells, 3 mice. (Right) Average relative response amplitude at the two pairing locations (Location 1: 0.75± 0.061, p1 = 1.45×10^{-4}; Location 2: 0.73±0.086, p2= 0.003, Wilcoxon Signed Rank Sum test, bar plots are mean±SEM).

Figure 4: Cue cells have limited effect on the spatial activity of subsequent cells along the track.

A) Population vector correlations for all spatially tuned cells for normal middle cue laps and shifted cue laps. (1716 cells from 48 sessions). Locations of the middle and lap cue are shown blue and green shaded areas, respectively.

B) Numbers of spatially tuned cells, plotted based upon cross-correlation shift on shifted cue laps vs. position of peak firing on normal laps.

C) Mean number of non-shifting (i.e. non-cue, shift mag.<0.05m) and shifting cue cells (shift mag. 0.5m+/-0.1m) at each track position. Note that cue influenced cells are largely confined to locations right around the cue itself. Also note that there is an enrichment of non-shifting “place” cells immediately preceding the middle cue (black bump in middle).

D) Decoding of 4 normal, 1 cue shifted laps for a representative session. Each row represents 1 sec bin, the background (heatmap) colors show decoder posterior probability that the population neuron firing rate data represented a given location (y-axis) at a given 1s bin (x-axis). The magenta line shows the path along the maximum posterior probability (predicted position) at each bin, while the green line shows the observed position of the animal.

D) Decoding error for normal, cue shifted and omitted laps, calculated as the absolute median distance between the decoded value in each time bin and the actual value of the position.

bioRxiv preprint doi: https://doi.org/10.1101/2020.02.13.947903; this version posted February 13, 2020. The copyright holder for this preprint (which was not certified by peer review) is the author/funder. All rights reserved. No reuse allowed without permission.

χ^2=32.22, p<0.0001, $P_{Normal\text{-}Shift}$ <0.0001, $P_{Normal\text{-}Omit}$ <0.0001, $P_{Shift\text{-}Omit}$ =0.9999, Kruskal Wallis test and Dunn's multiple comparisons tests (n=60 sessions). Boxes, 25th to 75th percentiles; bars, median; whiskers, 99% range. *P*****<0.0001.

E) Decoding error for each treadmill position in normal and cue shifted laps, shaded error region represents the difference of the median from the null distribution of median decoder error. See also Fig. S4.

Supplementary Figure Legends

Figure S1. Related to Figure 1. Representations of sensory cues and place in the dentate gyrus

A-C) Comparison of cell firing for self-driven vs. motor driver treadmill. **A)** Fraction of active cells that are spatially tuned (with at least 0.001 transients per s) in mice advancing the treadmill belt through self-driven locomotion (black, 190 spatially tuned neurons in 5 mice, 1 session/mouse) and mice running on the motorized treadmill (red, 285 spatially tuned neurons in 8 mice, 1 session/mouse,) p=0.435, Wilcoxon Rank Sum test.

B) Firing rate of spatially tuned cells in self-driven vs. motorized treadmill (p=0.1876, Wilcoxon Rank Sum test).

C) Z scored spatial information in mice running on motorized treadmill and self-driven locomotion (p<0.0001, Wilcoxon Rank Sum test).

D) Mean spatial information by position. Non-normalized spatial information in spatial bins (10cm wide) along the treadmill during on-line cue manipulation task; location of the discrete cues are shown in green and blue shaded areas.

E) Firing of DG neurons in response to LED visual cue. Top: Location of lap cue (green boxes) and an LED cue (red box), during normal and omit trials. Bottom: spatial tuning heatmaps of 188 spatially tuned neurons (n=6 mice) during their first exposure to the middle cue on normal (left), and cue-omitted (right) laps.

F) Firing of DG neurons in response to whisker tactile cue. Top: Location of lap cue (green boxes) and a whisker tactile cue (brown box), during normal and omit trials. Bottom: spatial tuning heatmaps of 199 spatially tuned neurons (n=8 mice) during their first exposure to the middle cue on normal (left), and cue-omitted (right) laps. Each row represents a cell, and the x axis represents the treadmill position.

G) Average firing rate by position of neurons shown in panel E (LED cue) on normal (black, mean ± SEM), and cue-omitted (blue) laps plotted as a function of position on the linearized treadmill. Inset shows the averaged area under the firing rate curves (Hz*cm) within the visual cue region during normal laps (black bar) compared to the same region during cue omitted laps (blue bar, p<0.0001, Wilcoxon Signed Rank Sum test).

H) Average firing rates of neurons shown in panel F (tactile cue) on normal (black), and cue-omitted (blue) laps plotted as a function of position on the linearized treadmill. Inset shows the averaged area under the firing rate curves (Hz*cm) within the tactile cue region during normal laps (black bar representing blue area under the middle region of the treadmill) compared to the same region during cue omitted laps (blue bar, p<0.0001, Wilcoxon Signed Rank Sum test).

I) Fraction of inactive cells (gray), active cells (with at least 0.001 transients per s, pink) and spatially tuned cells (n_{total}=5054 cells from 8 mice 2 sessions each, mean=631.68±11.9).

bioRxiv preprint doi: https://doi.org/10.1101/2020.02.13.947903; this version posted February 13, 2020. The copyright holder for this preprint (which was not certified by peer review) is the author/funder. All rights reserved. No reuse allowed without permission.

J) Fraction of functional cell types classified based on their peak firing position selectivity among all spatially selective neurons.
K) A representative DG field of view of GCaMP6s-labelled population including spatially scattered odor (blue), lap (green) cue cells and place cells (orange).
L) Cumulative distribution curve of the firing rate of odor cue, lap cue and place cells; χ^2=2.901, p=0.2345, $P_{OdorCue\text{-}LapCue}$=0.2790, $P_{OdorCue\text{-}Place}$>0.9999, $P_{LapCue\text{-}Place}$>0.9999; $N_{OdorCue}$=114, N_{LapCue}=220, $N_{PlaceCell}$=114, from 8 mice 2 sessions each. Red dotted lines in violin plots show median, black dotted lines show quartiles. Comparisons are Kruskal Wallis and Dunn's multiple comparisons tests.

Figure S2. Related to Figure 2. Multisession tracking of single cue and place cells
A) Representative alignment of spatial footprints for cells segmented across individual sessions in a day or within days in a single imaging field.
B) Distribution of centroid distances between registered (blue, 1.45 ± 0.97, n=1604) and non-registered (pink, 7.07 ± 1.5, n=2214) neighboring cell pairs (p=6.9 10^{-43}, Wilcoxon Rank Sum test).
C) Fraction of all spatially tuned cells in day 1 session1 (D1), day 1 session 2 (D1') and day 7 (D7) that are registered to at least one other session, χ^2=0.25, p=0.9674, $P_{D1\text{-}D1'}$>0.9999, $P_{D1\text{-}D7}$>0.9999, $P_{D1'\text{-}D7}$>0.9999, n=8 matched sessions, Friedman and Dunn's multiple comparisons tests.
D) Comparison of average firing rates in all spatially tuned cells across days regardless of tracking χ^2=4.993, p=0.0824, $P_{D1\text{-}D1'}$ >0.9999, $P_{D1\text{-}D7}$ =0.0781, $P_{D1'\text{-}D7}$ =0.4789, N_{D1} =417, $N_{D1'}$ =365, N_{D7}=338, from 8 matched sessions, Kruskal Wallis and Dunn's multiple comparisons tests .
E) Representative field of view with odor cue cells (blue), lap cue cells (green), and place cells (orange) tracked within a day and across days.
F) Representative Ca^{2+} transients for an odor cue cell that has stable cue selective activity within one day and over 1wk (left). Transients for a place cell show relatively stable firing selectivity within day but a reorganization of firing selectivity across days (right). Black and red traces represent normal and cue shifted laps, respectively.
G) Firing rates of tracked neurons in visual and whisker tactile cue sessions ordered according to the position of peak activity in olfactory cue sessions (n=157 cells, 6 mice).
H) (Left) Scatter of z-scored middle cue cell Ca^{2+} amplitudes in normal vs cue-shifted laps (n=894 mid-cue cells, 64 sessions, 8 mice). Yellow line, diagonal. (Right) Averaged z-scored amplitudes of mid cue cells in shift (green) and normal (blue) laps, p=3.39×10^{-16}, Wilcoxon Signed Rank Sum test.

FigureS3. Related to Figure3. Suppression of diverse types of DG responses during cue presentation
A) Average firing rates around the middle cue, compared with out-of-field firing rates in the cue region. The position of the peak of firing within the spatial field of tuned cells precedes the nadir of out of field firing during normal cue laps. Blue shaded area shows the cue delivery position.
B) Session averaged excitatory (within-field) peak position vs. inhibitory (out-of-field) peak position (76 sessions). Red = avg., diagonal (yellow line).
C) Quantification of the position of excitation peak compared to the position of inhibition peak, p<0.01, Wilcoxon Signed Rank Sum test.

bioRxiv preprint doi: https://doi.org/10.1101/2020.02.13.947903; this version posted February 13, 2020. The copyright holder for this preprint (which was not certified by peer review) is the author/funder. All rights reserved. No reuse allowed without permission.

FigureS4. Related to Figure4. Effect of cue cells on the spatial coding along the track

A) Population vector correlations for all spatially tuned cells in each treadmill position for normal middle cue laps and omitted cue laps. (2657 cells from 54 sessions). Locations of the middle and lap cue are shown blue and green shaded areas, respectively.

B) Color histogram of spatially tuned cells, plotted based upon spatial field location and difference in firing rate between normal cue and cue-omitted laps.

C) Average difference in normal middle cue and cue-omitted lap firing rates based upon cell place field location. Note that the largest cue effects are confined to cells immediately responsive to the middle cue. With respect to pre-cue cells, Wilcoxon Rank Sum test: *** = $p < 10e-10$, * = $p = 0.03$, N.S.= not significant.

D) Cumulative distribution functions of the error of the maximum likelihood estimate of position for 30 recording sessions.

E) The decoder error for spatially tuned neurons plotted against their firing rate.

F) Decoding error for each treadmill position in normal and cue omitted laps, shaded error region represents the difference of the median from the null distribution of median decoder error.

G) Difference in decoder error in cue omitted laps from normal cue laps (blue) and cue shifted laps from normal cue laps (red), shows that decoder error in laps in which middle cue was manipulated, converged to that of normal laps, well before the subsequent lap cue.